SUCCESSIVE BIFURCATIONS AND VARIABILITY OF WIND-DRIVEN OCEAN FLOWS

Henk A. Dijkstra*
Department of Atmospheric Science
Colorado State University
Fort Collins, Colorado 80526, USA
dijkstra@atmos.colostate.edu

ABSTRACT

An overview is provided of recent results on patterns of internal variability of the midlatitude wind-driven ocean circulation. This variability arises through successive instabilities of these flows. Bifurcation diagrams are presented for single-layer flows and physical mechanisms associated with some of the instabilities are briefly described. A homoclinic bifurcation is central for the low-frequency, aperiodic variability in these flows. The different flow regimes, as found in transient flow computations in both single- and multi-layer flows, can be interpreted with help of the bifurcation diagrams.

INTRODUCTION

The large-scale ocean circulation is driven both by momentum fluxes, as well as by fluxes of heat and freshwater at the ocean–atmosphere interface. The near-surface circulation is dominated by horizontal currents that are mainly driven by the wind-stress forcing, while the much slower motions of the deep ocean are mainly induced by buoyancy differences. Figure 1 gives an impression of the near-surface flow in the northwestern part of the North Atlantic basin, based on a multi-pass satellite image of the sea-surface temperature (SST) field.

The wind-stress curl induced by the easterly winds in very low and very high latitudes, on the one hand, and the midlatitude westerlies, on the other, induces midlatitude cellular flows, called gyres. The North Atlantic is typical of several other ocean basins in exhibiting a dominant anticyclonic cell, called the subtropical gyre, and a smaller cyclonic cell, called the subpolar gyre (Fig. 1). Each of these gyres has a narrow, fast-flowing western boundary current and a slower, more diffuse eastern boundary current. The major surface current is the Gulf Stream, an eastward jet that arises through the merging of the two western boundary currents, the northward-flowing Florida Current and the southward flowing Labrador Current.

The variability of the Gulf Stream has been studied for decades through time-continuous in situ measurements, at a few locations, as well as by more detailed one-time-only hydrographic surveys. As the Gulf Stream penetrates further east into the open ocean, it spreads out due to meandering. In this region, cut-off eddies are formed and move away from the main jet, generally in a westward or southwestward direction. Their average wavelength is about 100 km and their propagation speed is of the order of 10 km/day. The scale of the eddies is related to an internal length scale of the ocean, the internal Rossby deformation radius (Pedlosky, 1987); both stratification and rotation effects contribute to define this radius. In the oceans, motions with this horizontal scale are commonly referred to as mesoscale. Generally, the presence of mesoscale eddies causes variability on a subannual, 2–3-month time scale.

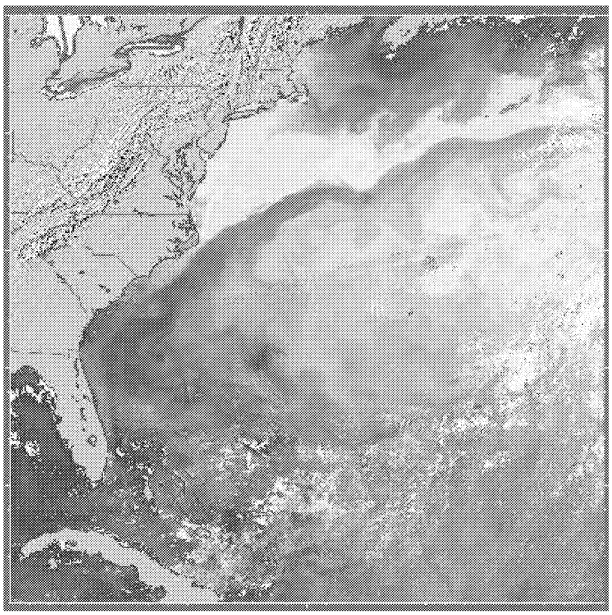

Figure 1: *Composite, multi-pass satellite image of the average SST field in May 1996 within the Gulf Stream region. The infrared data used to obtain this picture were obtained from high-resolution (0.5° horizontally) observations from the Advanced Very High Resolution Radiometer (AVHRR, see http://fermi.jhuapl.edu/avhrr/index.html). The dark shading indicates a warm sea surface, with SSTs of typically 25° C in the Gulf of Mexico and the Florida Straits; lighter shading indicates a colder sea surface.*

The last decade has seen a huge increase in the observational information available on the oceans' basin and global scales (WOCE, 2001). As a result, attention has focused more and more on the temporal variability of the wind-driven circulation that is associated with larger spatial scales and involves lower frequencies. Various observations — though limited in spatial and temporal coverage — suggest the existence of distinct scales of temporal variability from subannual (Lee and Cornillon, 1995), through seasonal (Schott and Molinari, 1996)

*Also at: Institute for Marine and Atmospheric research, Utrecht, Department of Physics and Astronomy, Utrecht University, Utrecht (IMAU), the Netherlands

to interannual (Auer, 1987) scales.

The sources of this low-frequency variability and of the associated spatio-temporal patterns have become an object of intense scrutiny. The classical view is that the overall red spectrum of the oceans' variability in time is due to its "flywheel" integration of atmospheric white noise (Frankignoul and Hasselmann, 1977) and that any peaks that rise above this broad-band spectrum also result primarily from changes in the external forcing, especially in wind stress or buoyancy fluxes. The forced variability does not always account, however, for all or even most of the observed variability. Internal ocean dynamics — i.e., intrinsic variability due to nonlinear interactions between two or more physical processes that affect the wind-driven ocean circulation — may therefore play an important role on these time scales.

In this paper, an overview is given of results of internal variability of the wind-driven ocean circulation. Using dynamical systems theory, we will first analyze successive bifurcations in single-layer (constant density) models and next use these results to interpret flow regimes as found in multi-layer (stratified) models.

SINGLE-LAYER FLOWS

The theory of the homogeneous wind-driven ocean circulation (Sverdrup, 1947; Stommel, 1948; Munk, 1950) is one of the cornerstones in physical oceanography. This theory describes the mid-latitude wind-driven ocean flows in an active layer of ocean water with constant density ρ in an idealized $L \times B$ rectangular basin. Below this layer, with equilibrium thickness H, there is a very deep motionless layer of density $\rho + \Delta\rho$ (Fig. 2). The basin is located on a midlatitude β-plane with Coriolis parameter $f = f_0 + \beta_0 y$.

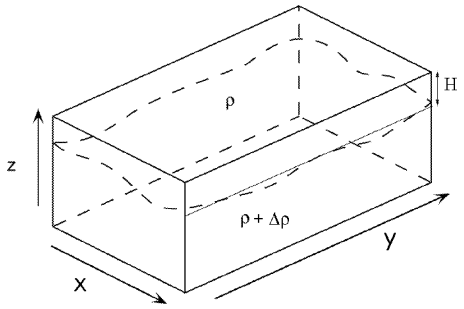

Figure 2: *Sketch of the ocean model set-up in a rectangular basin on a midlatitude β-plane.*

Let the flow be characterized by a horizontal length scale L and a horizontal velocity scale U. When the Rossby number $\epsilon = U/(f_0 L)$ is small, quasi-geostrophic theory is an adequate description of the large-scale flow (Pedlosky, 1987). Let ψ indicate the geostrophic streamfunction in the horizontal plane, then the zonal velocity u, the meridional velocity v and the vorticity ζ are given by $u = -\partial\psi/\partial y$, $v = \partial\psi/\partial x$ and $\zeta = \partial v/\partial x - \partial u/\partial y = \nabla^2\psi$, respectively. When the flow is driven by a zonal wind stress $\boldsymbol{\tau}$, the governing equation in this theory is the (equivalent) barotropic vorticity equation, given by

$$\frac{\partial q}{\partial t} + J(\psi, q) = A_H \nabla^4 \psi + \frac{\boldsymbol{\nabla} \times \boldsymbol{\tau}}{\rho_0 H} \qquad (1a)$$

$$q = \nabla^2 \psi - \frac{f_0^2}{H g'} \psi + \beta_0 y \qquad (1b)$$

Here, q is the potential vorticity, $g' = g\Delta\rho/\rho$ is the reduced gravity and the Jacobian operator J is defined as $J(F, G) = F_x G_y - F_y G_x$ where the subscripts indicate differentiation. The quantity A_H represents the turbulent lateral friction coefficient. The strict homogeneous case is obtained when the second layer is a solid, for which $g' \to \infty$. No-slip boundary conditions are usually prescribed at the east-west boundaries and slip conditions at the north-south boundaries, i.e.

$$x = 0, L \quad : \quad \psi = 0, \qquad \frac{\partial \psi}{\partial x} = 0 \qquad (2a)$$

$$y = 0, B \quad : \quad \psi = 0, \qquad \frac{\partial^2 \psi}{\partial y^2} = 0 \qquad (2b)$$

The wind-stress profile often considered with (1) is

$$\tau^x(x, y) = -\tau_0 \, (\sigma \cos \pi \frac{y}{B} + (1 - \sigma) \cos 2\pi \frac{y}{B}) \; ; \; \tau^y(x, y) = 0 \qquad (3)$$

where the dimensionless parameter σ controls the shape and τ_0 is a typical amplitude. Following Veronis (1963), much attention (Ierley and Sheremet, 1995) has focussed on the subtropical (single) gyre system as obtained above with the choice $\sigma = 1$. The single-gyre wind-stress forcing consists of easterlies (westerlies) at the south (north) part of the basin. The so-called double-gyre case has more recently received much attention and is obtained with $\sigma = 0$ in (3). In this case, both the subtropical and subpolar gyres are forced and the wind stress is symmetric with respect to the mid-axis of the basin (Fig. 3).

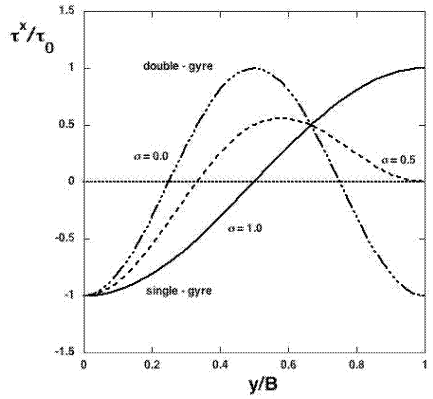

Figure 3: *Plots of the zonal wind stress (3) for three different values of σ.*

Under a given steady wind-stress forcing, the linear steady quasi-geostrophic theory predicts a Sverdrup interior flow and a frictional western boundary layer. The linear theory provides a first order explanation of the existence of western boundary currents, such as the Gulf Stream. The nonlinear theory is, however, far from complete. Although the strong effect of inertia on the flows was already shown by Veronis (1963), the work to determine systematically the solution structure of (1) versus the lateral friction parameter A_H did not start until the mid 1990s (Cessi and Ierley, 1995).

PRIMARY BIFURCATIONS

For large values of A_H, a unique and globally stable flow state for both single- and double-gyre cases is found (Dijkstra

Table 1: Standard values of parameters used in the computations

Parameter	Value	Parameter	Value
L	1.0×10^6 m	τ_0	1.5×10^{-1} Pa
H	6.0×10^2 m	β_0	1.6×10^{-11} $(\text{ms})^{-1}$
f_0	1.0×10^{-4} s^{-1}	U	1.6×10^{-2} ms^{-1}
ρ_0	10^3 kgm^{-3}	B	1.0×10^6 m

and De Ruijter, 1996). To investigate the solution structure of the equations when A_H is decreased, continuation methods (Dijkstra, 2000) have been used on discretized versions of (1). In the results below, a 128 x 128 equidistant grid is used and the steady states are computed versus $Re = UL/A_H$. In other studies, also the ratio of boundary layer thicknesses δ_I/δ_M, where $\delta_I = (U/\beta_0)^{1/2}$ and $\delta_I = (A_H/\beta_0)^{1/3}$ is used. Other parameters are fixed at values shown in Table 1 and $g' \to \infty$.

Single-gyre flows

In the bifurcation diagram (Fig. 4a) for the single-gyre flows ($\sigma = 1$), a value of the streamfunction at a certain gridpoint (ψ_R) is plotted versus Re. Each point on the curve represents a steady state and its stability is indicated by the linestyle, with solid (dashed) curves indicating stable (unstable) solutions. At small and large values of Re, there is a unique steady solution, while between the two-saddle node bifurcations L_1 and L_2 there is a regime of multiple equilibria. Plots of the streamfunction ψ at labelled locations in Fig. 4a are shown in Fig. 4b-d. The pattern in Fig. 4b near $Re = 10$ deviates already from the symmetric linear Munk-Sverdrup solution. The effects of strong nonlinearities on the flow can be seen in the streamfunction for both solutions at $Re = 60$. A strong north-south asymmetric solution (Fig. 4c) appears on the lower branch and a gyre filling up the basin (Fig. 4d) develops on the upper branch.

Double-gyre flows

For the case $\sigma = 0$, the structure of the steady solutions is shown through the bifurcation diagram in Fig. 5a, where the value of the streamfunction at a point in the southwest part of the domain (ψ_R) is plotted versus $Re = UL/A_H$. At large values of A_H (small Re), the anti-symmetric double-gyre flow (Fig. 5b) is a unique state. When lateral friction is decreased, this flow becomes unstable at the pitchfork bifurcation P_1 and two branches of stable asymmetric states appear for smaller values of A_H (larger Re). The solutions on these branches have the jet displaced either southward or northward (Fig. 5c) and are exactly symmetrically related for the same value of Re. For even smaller friction, the anti-symmetric flow becomes inertially dominated and ψ_R increases rapidly. A pitchfork bifurcation P_2 occurs on the anti-symmetric branch where an additional pair of asymmetric solution branches appear (Fig. 5d); all these solutions are unstable.

The existence of the bifurcation P_1 (Fig. 5a) captures the heart of the physics of symmetry breaking in these flows. The physical mechanism of the instability can be analyzed with help of the patterns of the steady state and the eigenvector of the linear stability analysis which has a zero growth

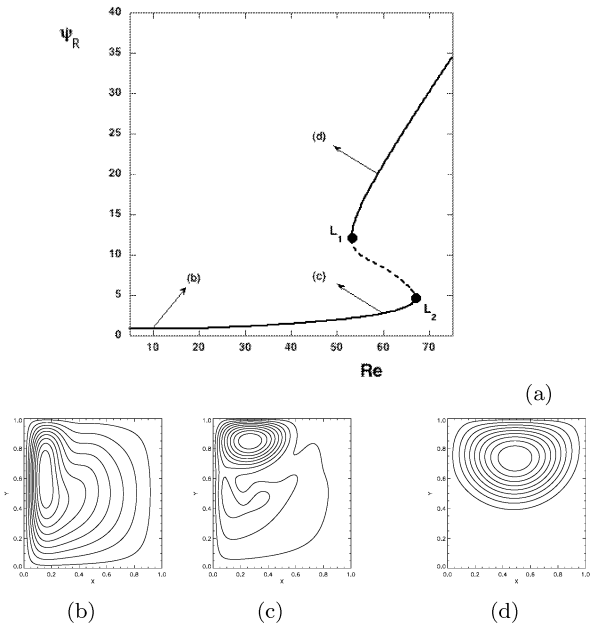

Figure 4: *(a) Bifurcation diagram for the single-gyre ($\sigma = 1$) barotropic quasi geostrophic model for a square basin with $Re = UL/A_H$ as the control parameter. (b) Pattern of ψ near $Re = 10$ on the lower stable branch in (a). (c) Same for $Re = 60$ along lower branch and (d) for $Re = 60$ along the upper stable branch.*

rate just at P_1. The streamfunction and vorticity field of the steady state are presented in Fig. 6a, while those of the streamfunction and vorticity perturbation (determined from the eigenvector) are shown in Fig. 6b. The streamfunction perturbation has a tripole-like structure with a negative vorticity center along the jet-axis and two positive vorticity centers at either side. The special property of these patterns is that the center negative vorticity lobe is exactly localized within the vorticity extrema of the anti-symmetric basic state. If we consider the region just above the symmetry line of the eastward jet ($y = 0.5$), the perturbation zonal flow is eastward, and therefore in the same direction as that of the basic state. More northward (above $y = 0.7$), the perturbation flow is westward and therefore also in the same direction as the steady flow. If we consider the flow just below the symmetry line of the steady jet, it is observed that the flow perturbations are in the opposite direction to that of the basic state. Hence, the flow perturbation weakens the subtropical gyre and strengthens the subpolar gyre. The asymmetric change in the strength of the basic flow due to the perturbations leads to increased horizontal shear in the eastward jet, which leads to an additional negative vorticity. This extra vorticity just amplifies the original perturbation flow in this region leading to instability.

Connection between single-gyre and double-gyre flows

We can follow the branches of the double-gyre case in the parameter σ (controlling the asymmetry of the wind stress) to connect to the single-gyre case. The bifurcation diagram for $\sigma = 0.1$ (Fig. 7a) shows the basic imperfections of the double-gyre flow. The branch S_1 connects to the branch A_{1u}; this is

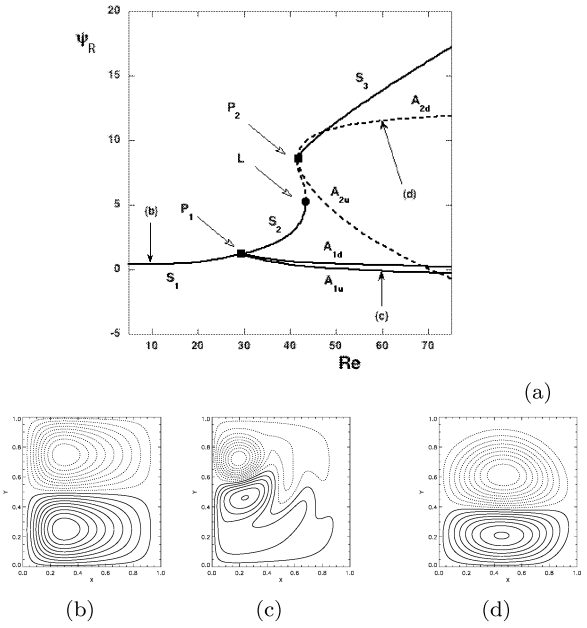

Figure 5: *(a) Bifurcation diagram for the double-gyre ($\sigma = 0$) barotropic quasi geostrophic model for a square basin with $Re = UL/A_H$ as the control parameter. (b) Pattern of ψ near $Re = 10$ on the lower stable branch in (a). (c) Same for $Re = 60$ along the branch A_{1u}; the pattern on the branch A_{1d} at $Re = 60$ is the mirror image of (c) with respect to reflection through the midaxis of the basin. (d) The pattern at $Re = 60$ on the branch A_{2d}.*

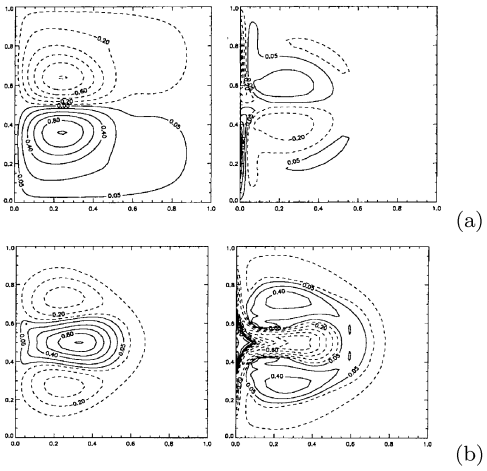

Figure 6: *(a) Contour plots of the steady state at the pitchfork bifurcation P_1 in Fig. 5a with the streamfunction ($\bar{\psi}$) in the left panel and the vorticity ($\bar{\zeta}$) in the right panel. (b) Contour plots of the perturbation destabilizing the steady state of (a) with the streamfunction ($\tilde{\psi}$) in the left panel and the vorticity ($\tilde{\zeta}$) in the right panel (from Dijkstra and Katsman (1997)).*

expected because the $\sigma = 0.1$ wind stress induces a preference for the jet-up solution. Both the branches containing jet-down solutions (the branches A_{1d} and A_{2d}) connect to the branch S_2 to give the branch labeled with $A_{1d} - S_2 - A_{2d}$ in Fig. 7a. The branch of jet-up solutions A_{2u} connects to the branch S_3 and forms the $S_3 - A_{2u}$ branch. When the wind stress is made more

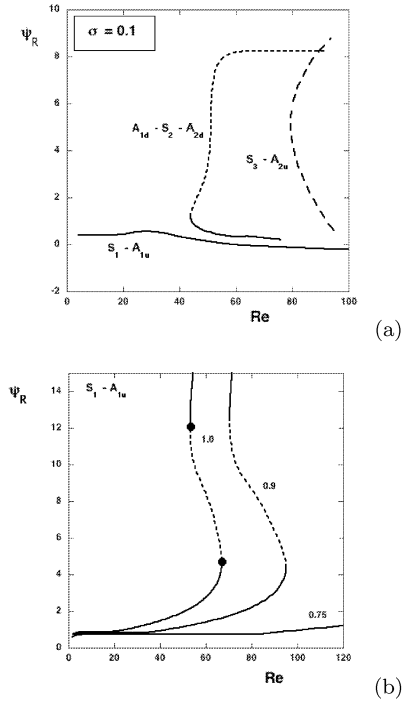

Figure 7: *(a) Bifurcation diagram for $\sigma = 0.1$ and (b) for several larger values of σ.*

asymmetric through an increase in σ, both the $A_{1d} - S_2 - A_{2d}$ and $S_3 - A_{2u}$ branches move quickly to higher values of Re and eventually move out of the computational domain. What remains is the $S_1 - A_{1u}$ branch. Up to $\sigma = 0.75$, there are no saddle-node bifurcations on this branch (Fig. 7b), but these appear for values of σ just before $\sigma = 0.9$. It is clear that the $S_1 - A_{1u}$ branch eventually deforms into the single branch of the single-gyre wind stress case ($\sigma = 1$).

SECONDARY BIFURCATIONS: DOUBLE-GYRE CASE

The secondary bifurcations of the single-gyre flows have been studied in detail by Sheremet *et al.* (1997) and time-dependent behavior of the single-gyre flows has also been studied extensively (Berloff and Meacham, 1997; Meacham and Berloff, 1997, 1998; Berloff and Meacham, 1998a). We will here only focus on the double-gyre case since it appears to be a better prototype situation for the actual North Atlantic Ocean circulation (Dijkstra, 2000).

Hopf bifurcations

The symmetry-breaking associated with the pitchfork bifurcation P_1 leads to two branches of stable asymmetric steady states. However, these states also become unstable at larger values of Re due to the occurrence of Hopf bifurcations. The pattern of the oscillatory mode which destabilizes the asymmetric double-gyre flow at each Hopf bifurcation can be de-

termined from the solution of the linear stability problem. At the Hopf bifurcation, a complex conjugate pair of eigenvalues $\sigma = \sigma_r \pm i\sigma_i$ crosses the imaginary axis. The corresponding complex eigenfunction $\hat{\mathbf{x}} = \hat{\mathbf{x}}_R + i\hat{\mathbf{x}}_I$ provides the disturbance structure $\Phi(t)$ with angular frequency σ_i and growth rate σ_r to which the steady state becomes unstable, i.e.,

$$\Phi(t) = e^{\sigma_r t}\,[\hat{\mathbf{x}}_R\ \cos(\sigma_i t) - \hat{\mathbf{x}}_I\ \sin(\sigma_i t)] \qquad (4)$$

Propagation features of a neutral eigenmode ($\sigma_r = 0.0$) can be determined by first looking at $\Phi(-\pi/(2\sigma_i)) = \hat{\mathbf{x}}_I$ and then at $\Phi(0) = \hat{\mathbf{x}}_R$. The period $\mathcal{P}$ of the oscillation is given by $\mathcal{P} = 2\pi/\sigma_i$.

The first Hopf bifurcation is associated with the destabilization due to a so-called Rossby-basin mode. These modes can be described by a sum of free Rossby waves where the coefficients are chosen such that the boundary conditions are satisfied. The simplest patterns of these modes can be determined by solving the normal mode problem for the motionless, unforced, non-viscous flow in (1). For the gravest Rossby basin mode, the period P is about 20 days. The pattern of this mode is shown in Fig. 8 at three instances during its propagation. The transition patterns at the Hopf bifurcations of

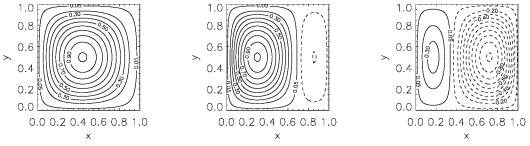

(a) (b) (c)

Figure 8: *Sketch of the streamfunction pattern of the gravest Rossby-basin mode at three different instances during its propagation. (a) $t/\mathcal{P} = 0$; (b) $t/\mathcal{P} = 1/4$; (c) $t/\mathcal{P} = 3/8$.*

the asymmetric double-gyre flows (near $Re = 52$ in Fig. 5a) are deformations of the pattern in Fig. 8. The growth rate of this mode is determined by the horizontal shear within the asymmetric double-gyre flow.

At the second Hopf bifurcation, the asymmetric state destabilizes to a mode which has an interannual period and the perturbations strengthen and weaken the eastward jet during both phases of the oscillation. These interannual, so-called gyre modes do not have their origin in the spectrum of the linear operator related to free Rossby-wave propagation. Simonnet and Dijkstra (2002) clarified the spectral origin of the gyre mode and presented a physical mechanism of its propagation. The gyre mode destabilizes the asymmetric solutions at a Hopf bifurcation located near $Re = 83$. The gyre mode, therefore has a negative growth factor σ_r for $Re < 83$ (Fig. 9). In the rightmost panels of Fig. 9, the patterns of the real and imaginary parts of this eigenmode ($\hat{\mathbf{x}}_R$ and $\hat{\mathbf{x}}_I$) are shown near $Re = 40$. The path of the gyre mode (the dash-dotted curve in Fig. 9) ends at the point M, where it splits into two stationary eigenmodes. These stationary modes exist up to the point P_1 where the asymmetric solutions cease to exist.

Also shown in Fig. 9 are the leading eigenmodes on the symmetric solution branch. The non-oscillatory mode responsible for the first pitchfork bifurcation (P_1) has a symmetric tripolar structure (Fig. 9, upper-left panel), similar to the streamfunction pattern in Fig. 6b and is called the P-mode. At P_1, the growth rate σ_r of this mode becomes positive which means that the symmetric steady flow becomes unstable to

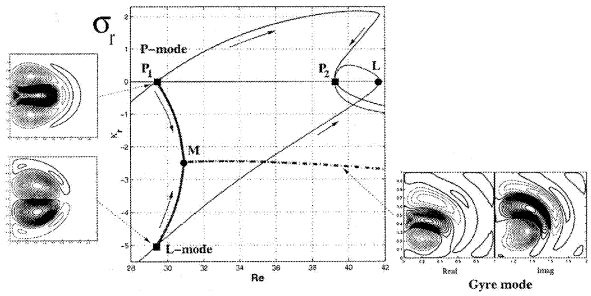

Figure 9: *Real part σ_r of the eigenvalues closest to the imaginary axis of the linear stability problem of the symmetric double-gyre flow (thin lines) and along one of the asymmetric steady states (thick lines). The P-mode (streamfunction pattern in the upper left panel) destabilizes the symmetric state at the pitchfork P (from Simonnet and Dijkstra (2002)). Along the asymmetric states, however, it deforms and merges with the L-mode (streamfunction pattern in the lower left panel) at the point M. This gives rise to the gyre mode (streamfunction patterns in the right panel).*

this perturbation pattern. The non-oscillatory mode responsible for the saddle-node bifurcation at L in Fig. 5a has a dipolar anti-symmetric structure (Fig. 9, lower-left panel). It thus acts on both gyres simultaneously so that they either increase or decrease in intensity. Simonnet and Dijkstra (2002) called this non-oscillatory mode the L-mode. At P_1, the L-mode is damped and σ_r becomes positive at the saddle-node bifurcation.

Relevant for the spectral origin of the gyre mode is the path of both the P-mode and L-mode on the asymmetric branches for $Re > 29.4$. For Re slightly above P_1, both modes are still non-oscillatory and have negative growth factor since the asymmetric branch is stable. The paths of the eigenvalues of both modes are indicated by the thick lines in Fig. 9 (starting at $Re = 29.4$). The growth factor of the P-mode decreases with Re, whereas that of the L-mode increases. Both modes meet at the point M (Fig. 9), which Simonnet and Dijkstra (2002) called the merging point, and give birth to the gyre mode.

Homoclinic bifurcations

We now consider the transient behavior of the double-gyre flows for values of Re beyond the first Hopf bifurcation. Trajectories computed for the 1000×1000 km basin show that indeed intermonthly variability first occurs with increasing Re in the form of periodic oscillations. Subsequently, when Re is increased, a quasi-periodic orbit is obtained with both interannual and intermonthly frequencies. Soon after $Re = 85$, the flow becomes irregular.

In Meacham (2000), transient flows in a basin of 1024×2048 km with no-slip boundary conditions on the lateral walls are considered. Transient solutions are computed versus lateral friction and either steady, periodic and aperiodic solutions are found. The structure of the steady states and periodic orbits can be understood with help of the bifurcation diagram Fig. 4a, where the periodic orbits are coming from the Hopf bifurcations. In some aperiodic solutions, large excursions are made and ultra low-frequency variability arises; Meacham (2000) suggests that it arises through a homoclinic orbit.

In Nadiga and Luce (2001), the location of the homoclinic orbit in the double-gyre flows is precisely located for flows in

a basin of size 1000×2000 km. Many transient computations are performed for different parameters and spectra are versus parameters. In this way, they find evidence for the occurrence of a homoclinic orbit of Shilnikov (1965) type. This behavior is characterized by specific periodic and aperiodic orbits that can be observed in the spectrum of the time series. Nadiga and Luce (2001) also demonstrated the importance of this dynamical phenomenon in explaining low-frequency variability in these flows.

For a 2560×2560 km basin, Chang *et al.* (2001) show that the anti-symmetric flow also destabilizes through a pitchfork bifurcation and that the asymmetric double-gyre flows subsequently destabilize through Hopf bifurcations. The first periodic orbit that appears has a subannual time scale and interannual variability occurs at slightly larger values of δ_I/δ_M. They monitor the transition to aperiodicity in detail by plotting the transport difference $\Delta\Phi$ between the subtropical and subpolar gyre versus the basin kinetic energy E of the flow for different ratios δ_I/δ_M (Fig. 10). The quantity $\Delta\Phi$ is defined as

$$\Delta\Phi = \frac{-\psi_{po} - \psi_{tr}}{\max \mid \psi \mid} \tag{5}$$

where $\psi_{po} < 0$ is the maximum transport of the subpolar gyre and $\psi_{tr} > 0$ the maximum transport of the subtropical gyre. Note that $\Delta\Phi = 0$ for an anti-symmetric flow, with $\psi_{po} = -\psi_{tr}$.

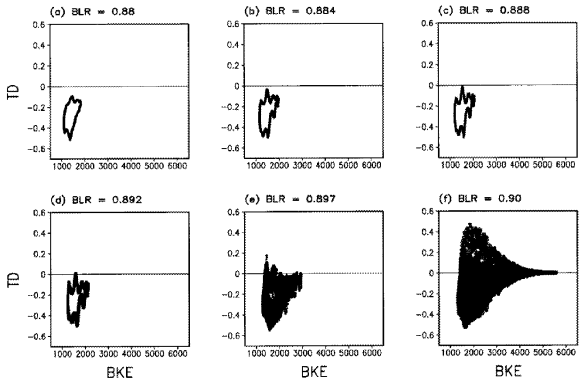

Figure 10: *Phase projections of trajectories computed by Chang* et al. *(2001). On the horizontal axis, the basin averaged kinetic energy (BKE) of the flow and on the vertical axis, the asymmetry of the flow measured through $TD = \Delta\Phi$ is plotted. The different panels are for several values of the ratio $BLR = \delta_I/\delta_M$. (a) 0.880, (b) 0.884, (c) 0.888, (d) 0.892, (e) 0.897 and (f) 0.900.*

In Fig. 10a, the projection of a periodic orbit around an asymmetric steady state can be seen and it has a period of about 148 days. As δ_I/δ_M increases, the periodic orbit at some instant of time reaches the symmetric double-gyre solution, for which $\Delta\Phi = 0$ (Fig. 10b-d). For slightly larger values the flow becomes aperiodic while the trajectory now attains both positive and negative values of $\Delta\Phi$ (Fig. 10e-f). It appears as though the periodic orbit makes a connection with the branch of steady symmetric solutions and then connects to the periodic orbit which is present around the symmetry-related asymmetric state: this is characteristic of the presence of a homoclinic bifurcation.

The connection between the pitchfork bifurcation, the gyre modes and the occurrence of the homoclinic bifurcation was clarified in Simonnet *et al.* (2005) and an overview of the bifurcation behavior leading to the homoclinic orbit is plotted in Fig. 11. The symmetry-breaking pitchfork bifurcation P is responsible for the asymmetric states; the P-mode is involved in this instability. The merging of the P-mode and the L-mode on the branches of the asymmetric states (at the points M) is responsible for the Hopf bifurcations H associated with the gyre modes. Finally, the periodic orbits arising from these Hopf bifurcation points on both asymmetric branches connect with the unstable anti-symmetric steady state at the point A; this gives rise to the homoclinic orbit. The type of homoclinic

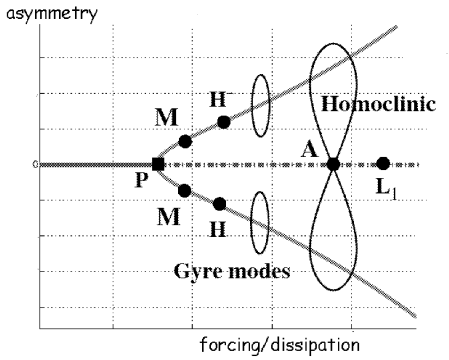

Figure 11: *Schematic bifurcation diagram of the solutions of the barotropic vorticity equation, plotted in terms of a measure of the asymmetry of the solution (for example, $\Delta\Phi$) versus either wind-stress intensity, the ratio δ_I/δ_M or simply the Reynolds number Re (from Simonnet* et al. *(2005)).*

orbit depends on the eigenvalues associated with the linear stability of the symmetric state at the connection point A (Wiggins, 1990). In case there are only real eigenvalues, there is a homoclinic connection of Lorenz-type and when the second and third eigenvalue form a complex-conjugate pair, there is a homoclinic bifurcation of Shilnikov type. Simonnet *et al.* (2005) show that both types can occur and that Shilnikov is more likely to occur at small lateral friction, in accordance with the results in Nadiga and Luce (2001).

LOW-FREQUENCY VARIABILITY

McCalpin and Haidvogel (1996) investigated the time-dependent solutions of (1) for a basin of realistic size (3600×2800 km), as well as the sensitivity of solutions to the magnitude of the wind stress and its meridional profile. They classified solutions according to their basin-averaged kinetic energy, and found three persistent states in their simulations (Fig. 12a). High-energy states are characterized by near-symmetry with respect to the mid-axis, weak meandering, and large jet penetration into the basin interior (Fig. 12b, left panel). Low-energy states have a strongly meandering jet that extends but a short way into the basin (Fig. 12b, right panel), while intermediate-energy states resemble the time-averaged flow and have a spatial pattern somewhere between high- and low-energy states (not shown). The persistence of the solutions near either state is irregular but can last for more than a decade of simulated time (Fig. 12a).

Primeau (1998) reproduces the time-dependent behavior of the flows found by McCalpin and Haidvogel (1996). By projecting the instantaneous flow fields onto four of the steady solutions, he found that a significant amount of the low-frequency variability of the trajectories are associated with

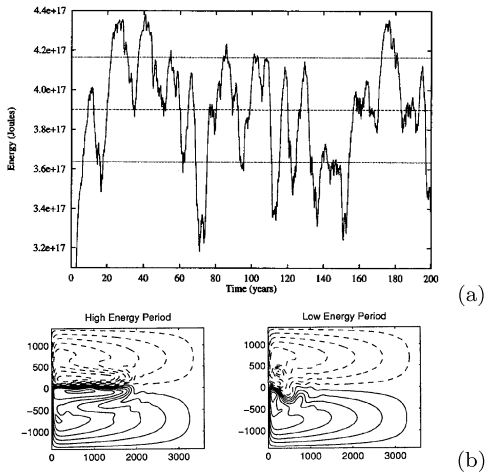

Figure 12: *(a) Typical variation of the basin averaged kinetic energy of the double-gyre flow in a large basin for the high-forcing or low-dissipation regime (from McCalpin and Haidvogel (1996)). (b) Typical patterns of the streamfunction for the high-energy state (left panel) and the low-energy state (right panel).*

transitions between these steady solutions. Furthermore, he explained that the reduction of the low-frequency variability associated with an increased asymmetry of the wind forcing is a result of the fact that some of the steady states cease to exist. However, knowing that there are many branches of steady solutions, many gyre modes and possibly several homoclinic connections, much more work is needed to figure out the precise dynamics causing the different energy states found in McCalpin and Haidvogel (1996).

At very high values of Re, Greatbatch and Nadiga (2000) analyze the flows for a 1000×2000 km basin and find that typically a four-gyre pattern arises in the mean flow. The upper and lower gyres (which circulate against the wind direction) are driven by mesoscale variability and are associated with a homogenization of potential vorticity (Salmon, 1998).

MULTI-LAYER FLOWS

We next consider a model with a more detailed representation of the stratification through the increase in the number of layers. In this three-layer model, the stratification is idealized by three stacked layers of water with constant densities ρ_i, $\rho_1 < \rho_2 < \rho_3$, and mean layer thicknesses H_i, with $H = H_1 + H_2 + H_3$. The governing equations of the model are

$$\frac{\partial q_1}{\partial t} + J(\psi_1, q_1) = A_H \nabla^4 \psi_1 + \frac{\boldsymbol{\nabla} \times \boldsymbol{\tau}}{\rho_0 H_1} \tag{6a}$$

$$q_1 = \nabla^2 \psi_1 - \frac{f_0}{H_1} h_1 + \beta_0 y$$

$$\frac{\partial q_2}{\partial t} + J(\psi_2, q_2) = A_H \nabla^4 \psi_2 \tag{6b}$$

$$q_2 = \nabla^2 \psi_2 - \frac{f_0}{H_2}(h_2 - h_1) + \beta_0 y$$

$$\frac{\partial q_3}{\partial t} + J(\psi_3, q_3) = A_H \nabla^4 \psi_3 \tag{6c}$$

$$q_3 = \nabla^2 \psi_3 + \frac{f_0}{H_3} h_2 + \beta_0 y$$

where the q_i represent the potential vorticity and the ψ_i the streamfunction in layer i. The quantities h_i represent interface perturbations related to the streamfunctions, ψ_i, through $h_i = f_0(\psi_i - \psi_{i+1})/g'_i$ for $i = 1, 2$, in which the $g'_i = g(\rho_{i+1} - \rho_i)/\rho_0$ represent the reduced gravity parameters. Conditions of no normal flow and no-slip, $\psi_i = 0$ and $\partial\psi_i/\partial n = 0$, are applied to the lateral boundaries.

Because of the representation of vertical shear in this model, the flows become susceptible to baroclinic instabilities (Pedlosky, 1987) which show up in the bifurcation diagrams as additional Hopf bifurcations (Dijkstra and Katsman, 1997). The patterns of the eigenmodes are labeled classical baroclinic modes CB1, CB2, etc. Nauw *et al.* (2004) used the three-layer model to investigate the different flow regimes (in a 2000×2000 km basin) which appear when the lateral friction coefficient A_H is decreased from $A_H = 2400$ m^{2}s^{-1} to $A_H = 300$ m^{2}s^{-1}. Parameter values are as in Table 1 with additional parameter values $H_1 = 600$ m, $H_2 = 1400$ m, $H_3 = 2000$ m, $g'_1 = 0.02$ ms^{-2} and $g'_2 = 0.03$ ms^{-2}.

Four flow regimes are identified by the analysis of a combination of the maximum northward transport of the time-mean flow and the normalized transport difference between the subtropical and subpolar gyre ($\Delta\Phi$). In this case, $\Delta\Phi$ is defined as in (5) in which the streamfunction ψ is that of the depth averaged flow. With decreasing A_H, the regimes found are the viscous anti-symmetric regime (for $A_H \geq 2100$ m^{2}s^{-1}), the asymmetric regime (for $1400 \leq A_H \leq 2100$ m^{2}s^{-1}), the quasi-homoclinic regime (for $700 \leq A_H \leq 1400$ m^{2}s^{-1}) and the inertial anti-symmetric regime (for $A_H \leq 700$ m^{2}s^{-1}).

For four different values of A_H, the value of $\Delta\Phi$ is plotted versus time in Fig. 13 and time-mean plots of the barotropic transport streamfunction Ψ of the vertically averaged flow are shown in Fig. 14. The time-series of $\Delta\Phi$ in the viscous symmetric regime (Fig. 13a) displays a low-frequency modulation of a high-frequency signal, while the time-mean state (Fig. 14a) is anti-symmetric. A transition to an asymmetric regime occurs at smaller A_H and a typical time-series of $\Delta\Phi$ in that regime is shown in Fig. 13b. The value of $\Delta\Phi$ remains positive after a spin-up of slightly more than 25 years and the amplitude of the high-frequency oscillation changes on a decadal time-scale. The time-mean barotropic transport streamfunction is asymmetric and displays a jet-down solution (Fig. 14b) in correspondence with the positive value of $\Delta\Phi$.

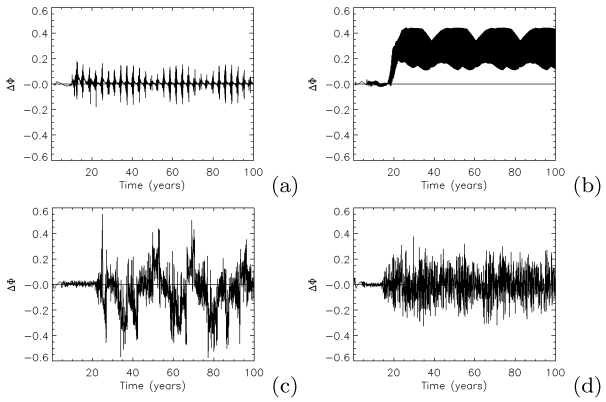

Figure 13: *Time series (including spin-up) of the transport difference, $\Delta\Phi$, for different values of A_H in the large basin case. (a) $A_H = 2400$ $m^2 s^{-1}$, viscous anti-symmetric regime; (b) $A_H = 1600$ $m^2 s^{-1}$, asymmetric regime; (c) $A_H = 900$ $m^2 s^{-1}$, quasi-homoclinic regime; (d) $A_H = 600$ $m^2 s^{-1}$, inertial anti-symmetric regime.*

For the flow in the quasi-homoclinic regime, several intervals can be distinguished in which there is a preference for either positive or negative values (Fig. 13c). The time-mean flow in this regime is slightly asymmetric (Fig. 14c). The time-series of the case in the inertial anti-symmetric regime (Fig. 13d) consists of a mainly high-frequency signal. The time-mean flow in this regime (Fig. 14b) is also anti-symmetric, but the midlatitude jet is much stronger than in the anti-symmetric viscous regime. Moreover, the large-scale gyres are accompanied by small-scale subgyres near the northern and southern boundary (Fig. 14d), similar to those in Greatbatch and Nadiga (2000).

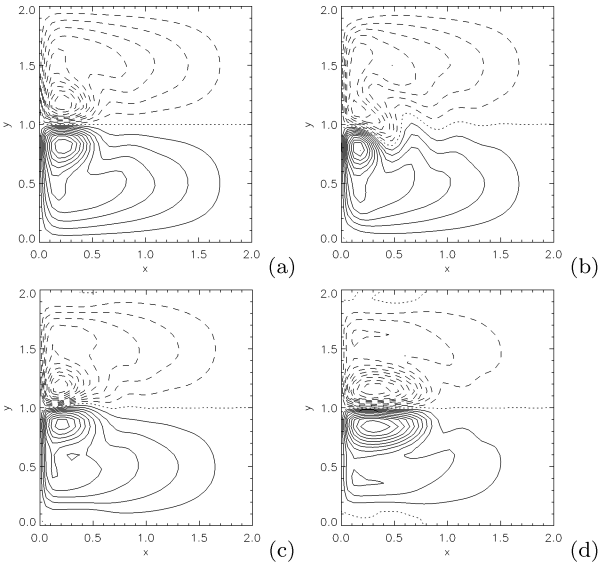

Figure 14: *The patterns of the barotropic transport function, Ψ, averaged over the final 75 years of integration for selected values of A_H. (a) A_H = 2400 $m^2 s^{-1}$, viscous symmetric regime; (b) A_H = 1600 $m^2 s^{-1}$, asymmetric regime; (c) A_H = 900 $m^2 s^{-1}$, quasi-homoclinic regime; (d) A_H = 600 $m^2 s^{-1}$, inertial symmetric regime.*

The four regimes are also characterized by different types of variability. In Nauw *et al.* (2004), the spatio-temporal variability of the flows (of which time series were shown for different values of A_H in Fig. 13) was analyzed with the M-SSA technique (Plaut *et al.*, 1995). In Fig. 15, a histogram is shown of the variance explained by each of the statistical modes, classified into groups that can be related to an internal mode. Case (a) is for a symmetric wind-stress forcing (σ = 0.0), while case (b) is for a slightly asymmetric wind stress ($\sigma > 0$). Most of the variance in the viscous anti-ymmetric regime can be explained by two classical baroclinic modes (CB1 and CB2), both with a period of about 3 months. In the inertial anti-symmetric regime, the variability is controlled by Rossby basin modes (RB) with intermonthly periods. Part of the variance in the asymmetric and quasi-homoclinic regimes can be explained by a gyre mode (G). It causes low-frequency variability with a period of about 3 years. The case with asymmetric wind-stress forcing demonstrates that the presence of the gyre mode is linked to the asymmetry of the time-mean state (Fig. 15b).

Nauw *et al.* (2004) also explain the transitions between the different regimes. The transition from the viscous anti-symmetric regime to the asymmetric regime is associated with

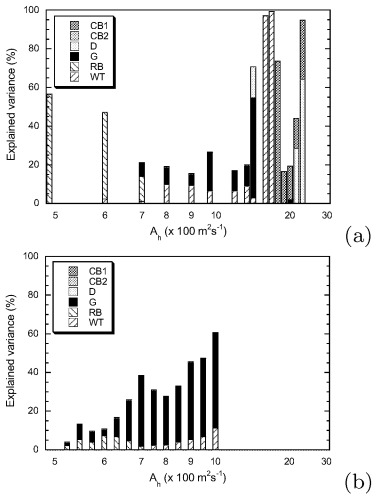

Figure 15: *Histograms of explained variances (%) for each of the different statistical oscillations, as determined from the M-SSA technique. (a) symmetric wind-stress forcing and (b) asymmetric wind-stress forcing. CB1 = classical baroclinic mode, causing meandering of the midlatitude jet; CB2 = classical baroclinic mode causing strengthening and weakening of the midlatitude jet; D = dipole oscillation; G = gyre mode; RB = Rossby basin mode; WT = wall-trapped mode. The D and WT modes are not discussed here.*

a symmetry-breaking pitchfork bifurcation. A homoclinic bifurcation, caused by the merging of two mirror-symmetric low-frequency relaxation oscillations and the unstable symmetric steady state, marks the transition from the asymmetric regime to the quasi-homoclinic regime. The transition from the quasi-homoclinic regime to the inertial anti-symmetric regime occurs through symmetrization of the zonal velocity field of the time-mean state. The interactions of high-frequency modes (such as CB1 and CB2) introduces forcing terms that oppose the wind-stress forcing, thereby moving the system towards a regime where both multiple equilibria and the gyre mode cease to exist. The results in Nauw *et al.* (2004) indicate that the study of the steady states, the bifurcations and the internal modes of variability provide an interpretation framework for complex time-dependent multi-layer flows. But, as the bifurcation diagrams become more complicated for 'realistic' size basins, much work is needed to obtain a more detailed dynamical interpretation of time-dependent flows in these basins.

Berloff and McWilliams (1999a) computed numerical solutions of the double-gyre flows in a two-layer model for five values of the lateral friction coefficient A_H in a basin of realistic size (3200 × 2800 km). For A_H = 1200 $m^2 s^{-1}$, an asymmetric steady state is found. At A_H = 1000 $m^2 s^{-1}$, quasi-periodic variability is found containing two dominant frequencies in the sub- and interannual range. The intermonthly variability is characterized by the presence of Rossby waves in the interior, while the interannual time-scale variability is associated with a fluctuating envelope surrounding a standing Rossby wave. At even smaller friction, a broadband spectrum appears, with the spectral power of the total energy increasing towards lower frequencies. At A_H = 800 $m^2 s^{-1}$, the behavior of the solutions is called 'chaotic', while at A_H = 600 $m^2 s^{-1}$ the flow patterns hover near three states with distinct total energy. These states are characterized by a different penetration length of the eastward jet and the

presence or absence of dipole-pattern oscillations in the recirculation region.

Characteristics of the asymmetric and quasi-homoclinic regimes are found in Berloff and McWilliams (1999a). The spatial pattern of the interannual mode in the symmetrically forced case at $A_H = 1000$ m^{2}s^{-1} (their Fig. 15) is similar to that of the gyre mode. The meridional position of the separation point of their time-dependent solution at $A_H = 600$ m^{2}s^{-1} alternates between locations to the north and to the south of the mid-axis of the basin on a decadal time-scale (their Fig. 18). This indicates an alternation between a jet-up and a jet-down solution and provides support for the nearby presence of a homoclinic orbit. Hence, this solution is likely to reside in a quasi-homoclinic regime. Berloff and McWilliams (1999b) investigate the double-gyre flows at even smaller values of A_H in a three-layer model and find a destabilization of the western boundary current at very small values of A_H.

In Siegel *et al.* (2001), flows for very small values of A_H are computed in a high resolution 6-layer model for a 3200 km square basin. In Fig. 16, upper layer streamfunction plots are shown from several numerical experiments differing in the values of A_H. The displayed sequence goes from relatively low Reynolds numbers *Re* (see definition in caption of Fig. 16) in

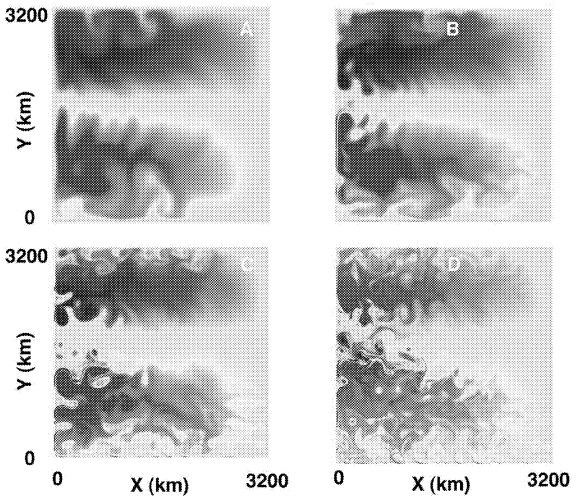

Figure 16: *Upper layer streamfunction snapshots of the ocean in a 3200 km square basin for varying Reynolds numbers, Re, with Re = 0.375, 1.5, 6.0, 24 for the panels (A)-(D), respectively. Here, Re = UL/A$_H$, with U = 10^{-3} ms^{-1} and L = 3200 km. The time-mean flow consists of an anticyclonic midlatitude subtropical gyre and a cyclonic subpolar gyre. The resolution in the computations increases from 25 km in (A) to 1.56 km in (D). Note the appearance of coherent vortices throughout the circulation in the highest value of Re results (from Siegel* et al. *(2001)).*

panel A to very high values in panel D. In panel D, numerous small-scale coherent vortices are displayed. Comparable features occasionally appear in the flow in panel C, but are essentially absent in the panels A and B. In C, the vortices are far sparser and do not survive for 'long' times (relative to vortex turnover time scales). The highest Re computations possess eddy kinetic energies approaching values like those observed in the open ocean. The dynamical origin of this so-called coherent vortex regime is still unknown.

SUMMARY AND OUTLOOK

With the dynamical systems approach as presented here, the idea is that an understanding of the physics of the observed complex ocean flows can be obtained by approaching the 'real' situation from particular limiting flows. One path proceeds from simple to complex situations through a hierarchy of models. We considered only single- and multilayer quasi-geostrophic models here, but the hierarchy is much larger including shallow-water models and primitive equation models. A second path was taken within one particular member of the model hierarchy where we proceeded from steady, highly-dissipative or weakly-forced flows to irregular, weakly dissipative or strongly forced flows by varying parameters, here only A_H.

By proceeding along both paths, two important issues have become apparent. The first issue is the existence of multiple steady flow patterns in wind-driven midlatitude ocean flows. These multiple states have been robust in the model hierarchy and their origin is a symmetry breaking shear instability, most apparent in the single-layer model. The second issue is that a classification of internal modes of variability is appearing. From a mathematical point of view, there are two types of modes. One type of modes, the Rossby-basin modes (RB), comes from the basic linear operator arising from the linear stability analysis of the no-flow state. The other types of modes (CB and G) do not have an origin in this basic linear operator. The oscillatory classical baroclinic modes (CB) arise when vertical shear is present in the background state. The low-frequency gyre modes (G) arise through a merger process of stationary modes. The gyre modes play an important role in the generation of aperiodic flows through the occurrence of homoclinic bifurcations.

It is less clear at the moment, why the transition behavior to aperiodic behavior differs in both single- and double-gyre flow. In Berloff and Meacham (1998b), it is suggested that the route to chaos in the baroclinic single-gyre case is the classical three-frequency route (Ruelle and Takens, 1970). which appears different from the Lorenz (Simonnet *et al.*, 2005) and Shilnikov (Nadiga and Luce, 2001) route (through a homoclinic connection) as found in double-gyre flows. The study of the route to complex flows over the model hiearchy, however, is in its infancy and many exciting new results can be expected in the near future.

*

References

Auer, S. J. (1987). Five-year climatological survey of the Gulf Stream system and its associated rings. *J. Geophys. Res.*, **92**, 11,709 – 11,726.

Berloff, P. S. and McWilliams, J. C. (1999a). Large-scale, low-frequency variability in wind-driven ocean gyres. *J. Phys. Oceanogr.*, **29**, 1925–1949.

Berloff, P. S. and McWilliams, J. C. (1999b). Quasi-geostrophic dynamics of the western boundary current. *J. Phys. Oceanogr.*, **29**, 2607–2634.

Berloff, P. S. and Meacham, S. P. (1997). The dynamics of an equivalent barotropic model of the wind-driven circulation. *J. Mar. Res.*, **55**, 407–451.

Berloff, P. S. and Meacham, S. P. (1998a). The dynamics of a simple baroclinic model of the wind-driven circulation. *J. Phys. Oceanogr.*, **28**, 361–388.

Berloff, P. S. and Meacham, S. P. (1998b). On the stability of the wind-driven circulation. *J. Mar. Res.*, **56**, 937–993.

Cessi, P. and Ierley, G. R. (1995). Symmetry-breaking multiple equilibria in quasi-geostrophic, wind-driven flows. *J. Phys. Oceanogr.*, **25**, 1196–1205.

Chang, K.-I., Ghil, M., Ide, K., and Lai, C.-C. A. (2001). Transition to aperiodic variability in a wind-driven double-gyre circulation model. *J. Phys. Oceanogr.*, **31**, 1260–1286.

Dijkstra, H. A. (2000). *Nonlinear Physical Oceanography: A Dynamical Systems Approach to the Large Scale Ocean Circulation and El Niño.* Kluwer Academic Publishers, Dordrecht, the Netherlands.

Dijkstra, H. A. and De Ruijter, W. P. M. (1996). Finite amplitude stability of the wind-driven ocean circulation. *Geophys. Astrophys. Fluid Dyn.*, **83**, 1–31.

Dijkstra, H. A. and Katsman, C. A. (1997). Temporal variability of the wind-driven quasi-geostrophic double gyre ocean circulation: Basic bifurcation diagrams. *Geophys. Astrophys. Fluid Dyn.*, **85**, 195–232.

Frankignoul, C. and Hasselmann, K. (1977). Stochastic climate models. II: Application to sea-surface temperature anomalies and thermocline variability. *Tellus*, **29**, 289–305.

Greatbatch, R. J. and Nadiga, B. (2000). Four-gyre circulation in a barotropic model with double-gyre wind forcing. *J. Phys. Oceanogr.*, **30**, 1461–1471.

Ierley, G. R. and Sheremet, V. A. (1995). Multiple solutions and advection-dominated flows in the wind-driven circulation. I: Slip. *J. Mar. Res.*, **53**, 703–737.

Lee, D. and Cornillon, P. (1995). Temporal variation of meandering intensity and domain-wide lateral oscillations of the Gulf Stream. *J. Geophys. Res.*, **100**, 13,603–13,613.

McCalpin, J. D. and Haidvogel, D. B. (1996). Phenomenology of the low-frequency variabiliity in a reduced gravity quasi-geostrophic double-gyre model. *J. Phys. Oceanogr.*, **26**, 739–752.

Meacham, S. P. (2000). Low frequency variability of the wind-driven circulation. *J. Phys. Oceanogr.*, **30**, 269–293.

Meacham, S. P. and Berloff, P. S. (1997). Instabilities of a steady, barotropic, wind-driven circulation. *J. Mar. Res.*, **55**, 885–913.

Meacham, S. P. and Berloff, P. S. (1998). Barotropic, wind-driven circulation in a small basin. *J. Mar. Res.*, **55**, 523–563.

Munk, W. (1950). On the wind-driven ocean circulation. *J. Meteorol.*, **7**, 79–93.

Nadiga, B. T. and Luce, B. (2001). Global bifurcation of Shilñikov type in a double-gyre model. *J. Phys. Oceanogr.*, **31**, 2669–2690.

Nauw, J., Dijkstra, H. A., and Simonnet, E. (2004). Regimes of low-frequency variability in a three-layer quasi-geostrophic model. *J. Mar. Res.*, **62**, 684–719.

Pedlosky, J. (1987). *Geophysical Fluid Dynamics. 2nd Edn.* Springer-Verlag, New York.

Plaut, G., Ghil, M., and Vautard, R. (1995). Interannual and interdecadal variability in 335 years of Central England Temperature. *Science*, **268**, 710–713.

Primeau, F. W. (1998). *Multiple Equilibria and Low-Frequency Variability of Wind-Driven Ocean Models.* Ph.D. thesis, M.I.T. and Woods Hole, Boston, MA, U.S.A.

Ruelle, D. and Takens, F. (1970). On the nature o turbulence. *Comm. Math. Phys.*, **20**, 167–192.

Salmon, R. (1998). *Lectures on Geophysical Fluid Dynamics.* Oxford Univ. Press, 400pp.

Schott, F. and Molinari, R. L. (1996). The western boundary circulation of the subtropical warm watersphere. In W. Krauss, editor, *The Warmwatersphere of the North Atlantic Ocean*, pages 229–252. Borntraeger, Berlin-Stuttgart, Germany.

Sheremet, V. A., Ierley, G. R., and Kamenkovich, V. M. (1997). Eigenanalysis of the two-dimensional wind-driven ocean circulation problem. *J. Mar. Res.*, **55**, 57–92.

Shilnikov, L. P. (1965). A case of the existence of a denumerable set of periodic motions. *Sov. Math. Dokl.*, **6**, 163–166.

Siegel, A., Weiss, J. B., Toomre, J., McWilliams, J. C., Berloff, P., and Yavneh, I. (2001). Eddies and coherent vortices in ocean basin dynamics. *Geophys. Res. Letters*, **28**, 3183–3186.

Simonnet, E. and Dijkstra, H. A. (2002). Spontaneous generation of low-frequency modes of variability in the wind-driven ocean circulation. *J. Phys. Oceanogr.*, **32**, 1747–1762.

Simonnet, E., Ghil, M., and Dijkstra, H. A. (2005). Homoclinic bifurcations of barotropic qg double-gyre flows. *J. Mar. Res.* sub judice.

Stommel, H. (1948). The westward intensification of wind-driven ocean currents. *Trans. Amer. Geophysical Union*, **29**, 202–206.

Sverdrup, H. U. (1947). Wind-driven currents in a baroclinic ocean with application to the equatorial current in the eastern Pacific. *Proc. Natl. Acad. Sci. Wash.*, **33**, 318–326.

Veronis, G. (1963). An analysis of the wind-driven ocean circulation with a limited number of Fourier components. *J. Atmos. Sci.*, **20**, 577–593.

Wiggins, S. (1990). *Introduction to Applied Nonlinear Dynamical Systems and Chaos.* Springer-Verlag, Heidelberg-Berlin, Germany.

WOCE (2001). *Ocean Circulation and Climate: Observing and Modeling the Global Ocean Ocean [Siedler, G. and Church, J. and Gould, J. (eds)].* Academic Press, San Diego, USA.